JOURNAL OF PROPULSION AND POWER
Vol. 34, No. 4, July–August 2018

Experimental Investigation on the Dynamic Icing Process over a Rotating Propeller Model

Yang Liu,* Linkai Li,† Zhe Ning,† Wei Tian,‡ and Hui Hu§
Iowa State University, Ames, Iowa 50011

DOI: 10.2514/1.B36748

An experimental study was conducted to investigate the dynamic ice accretion process over the blade surfaces of a rotating propeller model for unmanned-aerial-system (UAS) applications. In addition to revealing the transient ice accretion process over the rotating propeller surfaces, the dynamic thrust force generated by the propeller model was also measured simultaneously along with the required power inputs to drive the propeller model. Because of the combined effects of aerodynamics forces and the centrifugal force associated with the rotation motion, the ice accretion process over the rotating propeller surfaces was found to become very complicated. The ice accretion over the rotating propeller surfaces was found to become more preferable along the radial direction with the formation of lobster-tail-like ice structures extruding out from the propeller blade surfaces. The aerodynamic performance of the propeller model was also found to degrade tremendously due to the ice accretion, causing a significant reduction (i.e., up to 70% reduction) in mean thrust generation and a dramatic increase in force fluctuation amplitude (i.e., up to 250% increase). Despite of different types of ice accretion, the propeller model was always found to consume more power operating under icing conditions (i.e., up to 250% more power consumption under glaze icing conditions).

Nomenclature

A_c	=	ice accumulation parameter
a	=	total length of the mount and cone, m
$a1$	=	length of the mount, m
$a2$	=	length of the coniptical cone, m
C_P	=	power coefficient
C_T	=	thrust coefficient
D	=	diameter of the propeller, m
d	=	twice the leading-edge radius of airfoil, mm
d_{mount}	=	diameter of the mount tube, m
d_{support}	=	diameter of the supporting tube, m
F_c	=	centrifugal force, N
H	=	height of the propeller mount, m
H_{ice}	=	actual leading-edge ice thickness, mm
$H_{\text{ice,img}}$	=	imaged leading-edge ice thickness, mm
J	=	advance ratio of the propeller
LWC	=	liquid water content, g/m^3
m	=	water mass at a blade span location, kg
n	=	rotational speed of the propeller, rpm
P	=	power to drive the propeller, W
R	=	radius of the propeller, m
r	=	local rotational radius, m
T	=	thrust force acting on the propeller, N
T_∞	=	ambient temperature, °C
U	=	freestream velocity of airflow, m/s
u_{ice}	=	leading-edge ice growth rate, mm
V_1	=	local resultant velocity, m/s
V_2	=	local tangential velocity, m/s
α	=	effective angle of attack, deg
η	=	propeller efficiency
θ	=	twist angle of blade, deg
ρ	=	air density, kg/m^3
ρ_i	=	the ice density, kg/m^3
τ	=	duration of the ice accretion process, s
ω	=	angular speed of the propeller, rad/s

Received 30 April 2017; revision received 4 November 2017; accepted for publication 29 January 2018; published online 14 March 2018.

*Post-Doctoral Research Associate, Department of Aerospace Engineering, 2271 Howe Hall, Room 1200.

†Graduate Student, Department of Aerospace Engineering, 2271 Howe Hall, Room 1200.

‡Post-Doctoral Research Associate, Department of Aerospace Engineering, 2271 Howe Hall, Room 1200; currently Assistant Professor, School of Aerospace Engineering, Shanghai Jiaotong University, Shanghai, P.R. China.

§Martin C. Jischke Professor, Department of Aerospace Engineering, 2271 Howe Hall, Room 1200; huhui@iastate.edu. Associate Fellow AIAA (Corresponding Author).

I. Introduction

UNMANNED aerial system (UAS) is one of the most remarkable developments in aviation in recent years. These remotely—or sometimes autonomously—controlled aerial vehicles have become invaluable tools for various civilian and military applications, including reconnaissance and combat, cargo transport, search and rescue, scientific research, and wildfire monitoring. Free from having to accommodate the safety needs and endurance limits of onboard pilots, UAS is capable of flying extended missions and venturing into hazardous and remote locations [1]. Additionally, the associated cost savings and casualty reduction in using UAS for various military reconnaissance and surveillance operations are also very attractive, in comparison to conventional manned aircraft. As a result, military operations in the Balkans, Afghanistan, and Iraq have seen a widespread use of UASs such as Global Hawk, Predator, and Phoenix.

Icing is one common aviation danger that plagues both unmanned and manned aircraft flying in cold climate. Aircraft icing occurs when small, supercooled, airborne water droplets freeze upon impacting an airframe surface that allows formation of ice [2–4]. The freezing can be complete or partial, depending on how rapidly the latent heat of fusion can be released into the ambient air. When the ambient temperature is relatively cold (i.e., typically below −10°C [5]) and the airflow is relatively dry with a lower liquid water content (LWC), supercooled water droplets would freeze immediately upon impact onto the airframe surface, forming *rime* ice that closely follows the original airframe profiles due to the instantaneous freezing of the impinged water droplets. However, at temperatures just below the freezing point, if the LWC level in the airflow is relatively high, the impinged supercooled water droplets would not freeze completely, and the unfrozen water mass would run back along the airframe surface before freezing downstream, forming much complex ice shapes, which is called *glaze* ice. Because of its wet nature, glaze ice would form much more complicated ice shapes that are difficult to predict, and the resulting ice shapes tend to substantially deform the ice-accreting surface with the formation of "horns" and larger "feathers" growing outward into the airflow [6]. The irregular ice

shapes would severely decrease the aerodynamic performance of aircraft by causing large-scale flow separation, which can cause dramatic increases in drag and decreases in lift [7]. Mixed icing often occurs as a transition from rime to glaze conditions. Although noticeable research progress has been made in recent years [5,7–11], that is, evaluating aerodynamic degradation of iced airfoil/wing models [6,7,11], and characterization of surface water transport [10] and ice growth [8] driven by boundary-layer airflow, only simplified energy and mass transfer models have been developed for the ice accretion over airframe surfaces [8,9], and aircraft icing remains as an important unsolved problem at the top of the National Transportation Safety Board's most wanted list of aviation safety improvements.

In comparison with conventional, large-sized manned aircraft, lightweight UAS is more susceptible to inflight icing problems due to the lower cruising altitude with relatively higher LWC levels and warmer air temperatures, smaller excess power margin to offset the increased drag caused by ice accretion, lower flying velocity to result in longer exposing to icing conditions, and more damage to important sensors onboard [12]. The potential damage of inflight icing to UAS renders their operation unfeasible in cold weather. As described in Botura and Fahrner [13], 25% UAS flights encountered ice during a specific military action that has negatively impacted the success of the mission. The common icing avoidance strategies for UAS are keeping UAS on the ground [14] or modifying path planning [15], which would greatly reduce the operation capability of UAS in cold climate. This is particularly troubling for military UAS applications, in which icing conditions can lead to aborted missions and the loss of crucial tactical capabilities.

A number of studies were conducted in recent years to evaluate the effects of ice accretion on UAS operation capabilities. Siquig [16] conducted a comparative study with two different UAS (i.e., high-flying long-endurance UAS vs. low-flying short-endurance UAS) flying under icing condition in order to evaluate the effects of ice accretion on the UAS operation characteristics. Bottyán [17] developed an in-flight structural icing estimation method with a simple 2D ice accretion prediction model to investigate the effects of airflow temperature, LWC, airfoil geometry, and airflow speed on the ice accretion process over UAS wings. Szilder and McIlwain [14] evaluated the influence of Reynolds number on the ice accretion process over a NACA0012 airfoil for UAS applications. The regimes of rime and glaze formation as well as the ice accretion extent as a function of meteorological conditions were identified. Armanini et al. [18] proposed an icing-related decision-making system (IRDMS) to quantify in-flight icing based on changes in aircraft performance and measurements of environmental properties. Sørensen et al. [19] proposed to integrate a power control system and an electrically conductive carbon-nano-material-based coating for temperature control of UAS airfoil/wing surfaces in order to address the issue of structural change due to ice accretion.

Unlike most large manned aircraft using turbo jet engines for propulsion, almost all UAS are powered by propellers. Ice may accumulate on every exposed frontal surfaces of UAS, not only on fixed UAS wings, but also on rotating blades of propellers, which can significantly degrade the aerodynamic performance of the propellers. Surprisingly, although a number of studies were performed to address ice accretion and anti-/de-icing over UAS wings, very little can be found in the literature to quantify the dynamic ice accretion process and evaluate its effects on the resultant aerodynamic performance of rotating UAS propellers. In comparison to that over the surfaces of the fixed UAS wings, the dynamic ice accretion process over the surfaces of rotating UAS propeller blades would become even more complicated, due to the combined effects of aerodynamics shear forces and centrifugal forces.

It should be noted that a number of previous studies have been conducted to investigate icing phenomena over the surfaces of wind turbine and helicopter rotor blades [20–22]. As described in Palacios et al. [23], ice accretion over rotating wind turbine rotor blades is critically dangerous as it modifies the aerodynamic profiles of the blades, creates excessive vibration, increases weight and aerodynamic drag, and introduces mass and aerodynamic unbalance concerns as ice sheds off. Lamraoui et al. [24] found that uneven distribution of relative velocities along a rotor blade would cause a dramatic variation in ice accretion mass, with the maximum mass rate located on the outer section and the minimum near the blade root zone. Similar observation of a linear distribution of the accreted ice thickness along the rotor blade (i.e., a linear increase from the hub to the tip) was also reported by Fortin and Perron [25]. Such unbalanced three-dimensional mass distribution would drastically degrade aerodynamic performance and increase fatigue of the rotor blades. While the mass of rime ice accretion was dependent on blade span locations, the glaze ice growth was suggested to be even more complicated due to the surface water transport along the blade span as driven by the centrifugal forces [26]. In comparison to that over wind turbine rotors, the ice accretion on UAS propellers can be rather different due to the much lower operating Reynolds number, higher rotational speed, as well as the unique blade planform design and airfoil profiles adopted for UAS applications.

Advancing the technology for safer and more efficient UAS operations in atmospheric icing conditions requires the development of innovative, effective anti-/de-icing strategies tailored for UAS icing mitigation and protection. Doing so requires a keen understanding of the underlying physics of complicated thermal flow processes pertinent to UAS icing phenomena. With this in mind, we conducted an experimental study to quantify the dynamic ice accretion process over the rotating blades of UAS propellers in order to improve our understanding about the underlying icing physics. The experimental study was performed in the unique Icing Research Tunnel of Iowa State University (ISU-IRT) with a scaled UAS propeller model operated under a variety of icing conditions (i.e., ranged from dry rime to wet glaze icing conditions). In addition to achieving time-resolved measurements of the aerodynamic forces generated by the UAS propeller model in the course of the dynamic ice accretion process, a phase-locked imaging technique was also used to acquire the important features of the ice accretion process to quantify the dynamic ice accretion rate over the surfaces of the rotating UAS propeller blades. The time-resolved aerodynamic force measurements were correlated with the acquired ice accretion images to elucidate the underlying icing physics for the development of innovative, effective anti-/de-icing strategies tailored for UAS icing mitigation and protection.

II. Experimental Setup and Test Model

A. ISU-Icing Research Tunnel (ISU-IRT)

The experimental study was performed in the Icing Research Tunnel available at Aerospace Engineering Department of Iowa State University (i.e., ISU-IRT). ISU-IRT has a test section of 2.0 m in length × 0.4 m in width × 0.4 m in height with four side walls being optically transparent. ISU-IRT has a capacity of generating a maximum wind speed of 60 m/s and airflow temperature of −25°C. An array of 8 pneumatic atomizer/spray nozzles is installed at the entrance of the contraction section to inject microsized water droplets (10–100 μm in size) into the airflow. By manipulating the water flow rate through the spray nozzles, the LWC in ISU-IRT could be adjusted (i.e., LWC ranging from 0.1 to 5.0 g/m^3). In summary, ISU-IRT can be used to simulate atmospheric icing phenomena over a range of icing conditions (i.e., from dry rime to extremely wet glaze ice conditions).

B. Tested UAS Propeller Model

The test model used in the present study is a three-blade propeller, which is the most commonly used design for UAS applications. Figure 1 shows the schematic of the propeller model along with typical cross-section profiles of the rotor blades. While the radius of the rotor blades of the propeller is 100 mm (i.e., $R = 100$ mm), a coniptical spinner cone with a diameter of $D_{\text{cone}} = 33$ mm is designed at the center of the propeller. The rotor blades of the propeller have typical airfoil cross sections and platform profiles commonly used in modern propeller design. As shown schematically in Fig. 1a, two airfoil profiles (i.e., ARA-D 13% and ARA-D 20%) are used at different spanwise locations along the rotor blade: ARA-D 20% airfoil profile is used between $0.10R$ and $0.30R$, while the ARA-D 13% airfoil is used from $0.30R$ until the blade tip. With the prescribed blade platform profiles and twist angles (i.e., optimized based on the freestream airflow velocity and rotational speed of the propeller) as shown in

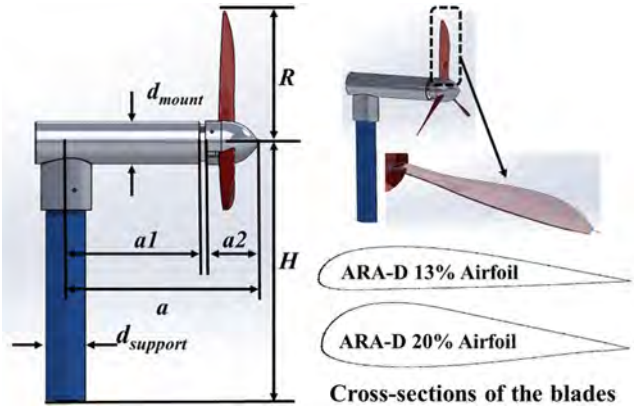

a) Propeller layout and rotor blades design

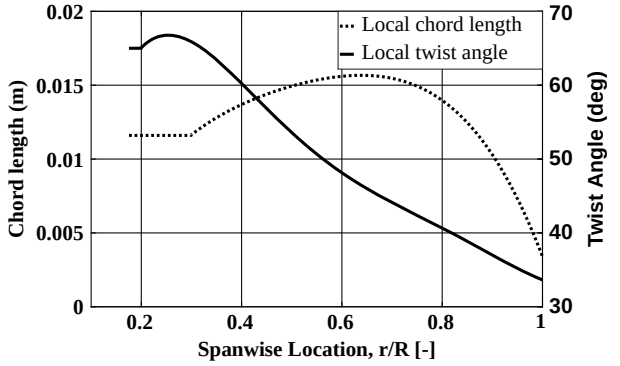

b) Chord length and twist angle along the blade

Fig. 1 Schematic of the UAS propeller model.

Fig. 1b, a spline function is used to interpolate the prescribed cross-section profiles in order to generate the three-dimensional geometry of the propeller blade using SolidWorks software. The primary design parameters of the propeller model are listed in Table 1.

The propeller model is made of a hard plastic material (i.e., VeroWhitePlus, RGD835 by Stratasys, Inc.), and was manufactured by using a rapid prototyping machine (i.e., 3D printer, Connex Object 260, with accuracy of 200 microns or better). The surfaces of the propeller blades were processed with fine sandpapers (i.e., up to 2000 grit) and special plastic polishes to achieve a very smooth, glossy finish. During the experiments, an aluminum tube with a streamlined cross section was used to support the propeller model in ISU-IRT. In the present study, with the radius of the rotor blades of the propeller being 100 mm, the blockage ratio of the propeller model (i.e., the ratio of the rotor blade sweeping area to that of ISU-IRT cross section) is 19.6%. Based on the findings described in Chen and Liou [27], the effects of the model blockage on the measurement results would be relatively small (i.e., <5%).

Figure 2 shows the schematic of the experimental setup used in the present study to quantify the dynamic ice accretion process over the rotating blades of the UAS propeller. In the present study, the rotor blades of the propeller model were driven by a brushless motor (DJI 2212, 940 KV), which was powered by a direct current (DC) power supply (VOLTEQ HY3050EX). During the experiments, the rotational speed of the model propeller was fixed at $n = 3000$ rpm by using a digital speed controller/manipulator to adjust the signal duty cycle of the brushless motor. In the meantime, the rotational speed of the propeller rotor was measured by a digital tachometer (MONARCH PLT200), which will generate a pulse signal from each rotation cycle of the propeller. The tachometer-generated pulse signal was then scanned by a 16-bit data acquisition system (NI USB-6218) and sent to a digital delay/pulse generator (BNC Model-577) to trig a high-resolution imaging system for phase-locked image acquisition of the ice accretion process over the rotating propeller blades. A proportional-integral-derivative (PID) algorithm (i.e., a control loop feedback mechanism) was formulated to achieve automatic rotational speed correction for the propeller rotor as a disturbance occurs (e.g., ice accretion or ice shedding). As a result, a speed control system with feedback compensation was integrated. With such a speed control system, when a speed reduction of the propeller was detected by the digital tachometer during the ice accretion experiment, more power would be provided instantly to the motor of the propeller model to bring its rational speed back to the prescribed value. The electric currents and voltages of the DC power supply applied to the brushless motor were also recorded, which can be used to determine the required power input for the UAS propeller model in the course of the dynamic ice accretion process.

In the present study, the aluminum supporting tube of the propeller model was connected to a high-sensitivity force-moment sensor (JR3 load cell, model 30E12A-I40) to measure the dynamic aerodynamic forces generated by the model propeller. The JR3 load cell, which is composed of foil strain gage bridges, is capable of achieving time-resolved measurements of forces and the moments (torques) about each axis. The precision of the JR3 load cell for force measurements is ±0.25% of the full range (40 N). During the experiments, the aerodynamic force data were sampled at a rate of 5000 Hz for each test case.

In addition to measuring the aerodynamic forces generated by the propeller model, a high-resolution imaging system was also used to record the dynamic ice accretion process over the surfaces of the rotating propeller blades under controlled environmental conditions. The image acquisition of the transient ice accretion process was achieved by using a high-speed camera (PCO Tech, PCO-Dimax S4, up to 1279 frames per second @ 2016 pixel by 2016 pixel) with a 50 mm Macro-lens (Nikon, 50 mm Nikkor 1.8D). The spatial resolution of the high-speed imaging results is 0.088 mm/pixel for the present study. During the experiments, the high-resolution imaging system was triggered by the digital delay/pulse generator (BNC Model-577) to achieve phase-locked image acquisition of the transient ice accretion process over the surfaces of the rotating propeller blades. A pair of 100 W Studio-LED light Units (RPS Studio Light, Model RS-5610 and RS-5620) were used in the present study to provide low-flicker illumination for the image acquisition.

III. Measurement Results and Discussion

A. Aerodynamic Performance of the UAS Propeller Model

The aerodynamic performance of a propeller is usually characterized by using the parameters of thrust coefficient (C_T), power coefficient (C_P), and propeller efficiency (η) [28]. These parameters are usually plotted against the advance ratio (J), that is, the ratio of the freestream velocity of airflow to the propeller tip speed. The definitions for the advance ratio, thrust, and power coefficients and propeller efficiency are given as follows:

$$J = \frac{V_\infty}{nD} \tag{1}$$

where V_∞ is the freestream velocity of the incoming airflow related to the propeller, n is rotational speed of the propeller, and D is the diameter of the propeller.

Table 1 Design parameters of the UAS propeller model

Parameter	R, mm	H, mm	d_{mount}, mm	d_{support}, mm	$a1$, mm	$a2$, mm	a, mm
Dimension	100.00	196.10	32.20	30.00	100.96	41.00	146.86

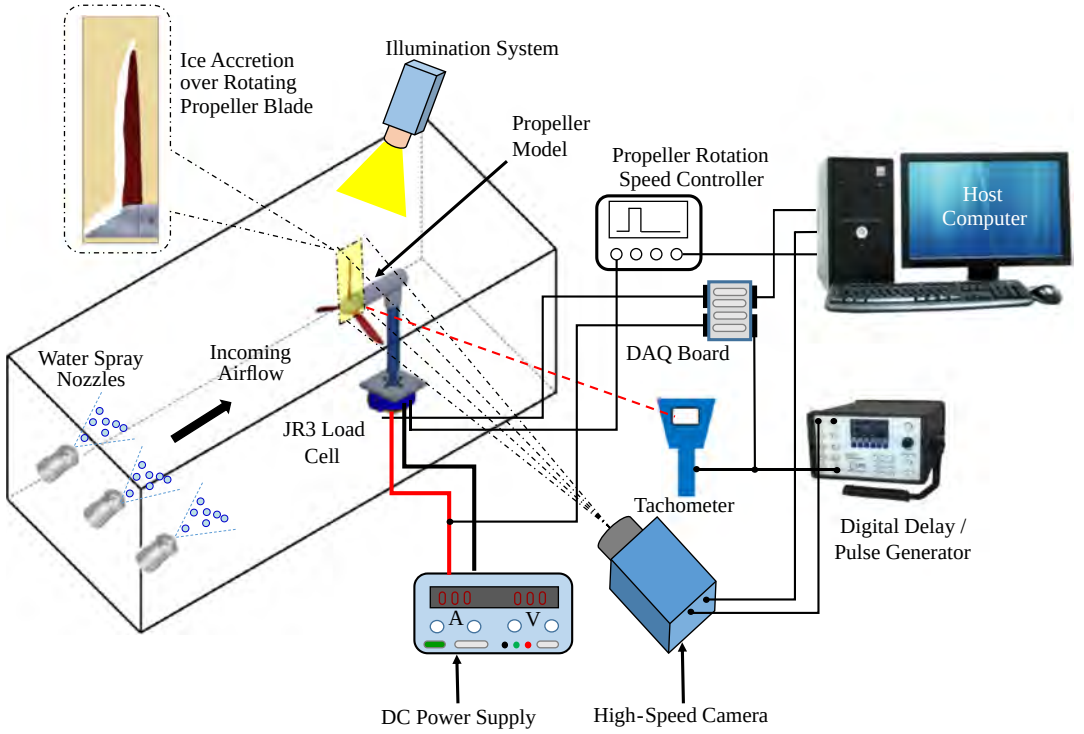

Fig. 2 Experimental setup for icing imaging, aerodynamic force, and power measurements.

$$C_T = \frac{T}{\rho n^2 D^4} \tag{2}$$

where T is thrust force generated by the propeller, and ρ is the air density.

$$C_P = \frac{P}{\rho n^3 D^5} \tag{3}$$

where P is the power input to drive the propeller.

$$\eta = J\frac{C_T}{C_P} \tag{4}$$

To determine the optimum advance ratio of the UAS propeller model used in the present study, a parametric study was performed by changing the freestream velocity of the incoming airflow in ISU-IRT, while the rotational speed of the propeller was kept as a constant (i.e., $n = 3000$ rpm for the present study). Figure 3 illustrates the measured aerodynamic performance of the UAS propeller model as a function of the advance ratio, J. As clearly shown in Fig. 3a, as the advance ratio of the propeller increases from 0.6 to 1.8, the thrust coefficient of the propeller, C_T, was found to decrease from 0.15 to 0.03 (i.e., decreasing by a factor of 5.0), whereas the power coefficient, C_P, was found to decrease from 0.4 to 0.1 (i.e., by a factor of 4.0). By using Eq. (4), the variation of the propeller efficiency as a function of the advance ratio was obtained, which is shown in Fig. 3b. It can be seen that, as the advance ratio increases from $J = 0.6$ to $J = 1.6$, the propeller efficiency was found to increase continuously and reach its maximum value at $J = 1.6$. When the advance ratio is further increased beyond $J = 1.6$, the propeller efficiency would begin to decrease, and has a dramatic drop at $J > 1.7$. Therefore, the optimum advance ratio for the UAS propeller model used in the present study was found to be $J = 1.6$., which is in the operation range of typical UAS propellers as given in Gur and Rosen [29] (i.e., J varies from 0.1 to 4.4).

For all the ice accretion measurement results given in the present study, the propeller model was operated at the advance ratio of $J = 1.6$ (i.e., with the freestream airflow velocity being set at $V_\infty = 16$ m/s and the rotational speed of the propeller rotors at $n = 3000$ rpm). Based on the intermittent maximum atmospheric icing conditions as described in FAA icing standard of 14 CFR Part 25 Appendix C [30], the effects of the ambient temperature (i.e., varied form $T_\infty = -15$ to -5°C) and LWC of the incoming airflow (i.e., varied form LWC = 0.5 to 2.0 g/m^3) on the ice accretions process were examined in detail.

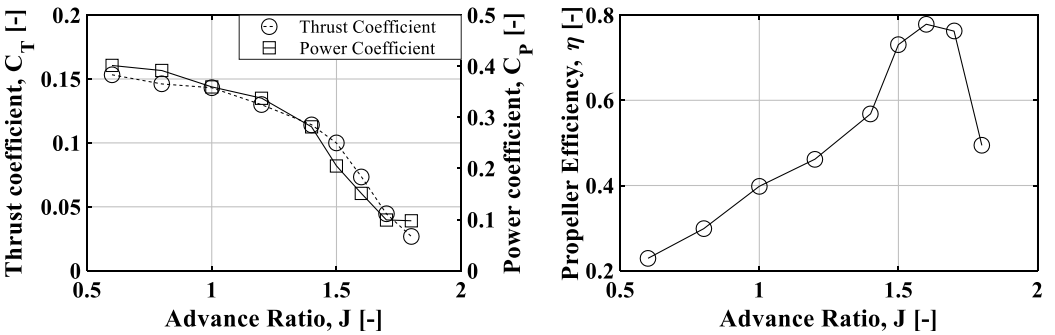

a) Thrust and power coefficients *vs.* advance ratio **b) Propeller efficiency *vs.* advance ratio**

Fig. 3 Performance of the UAS propeller model without ice accretion.

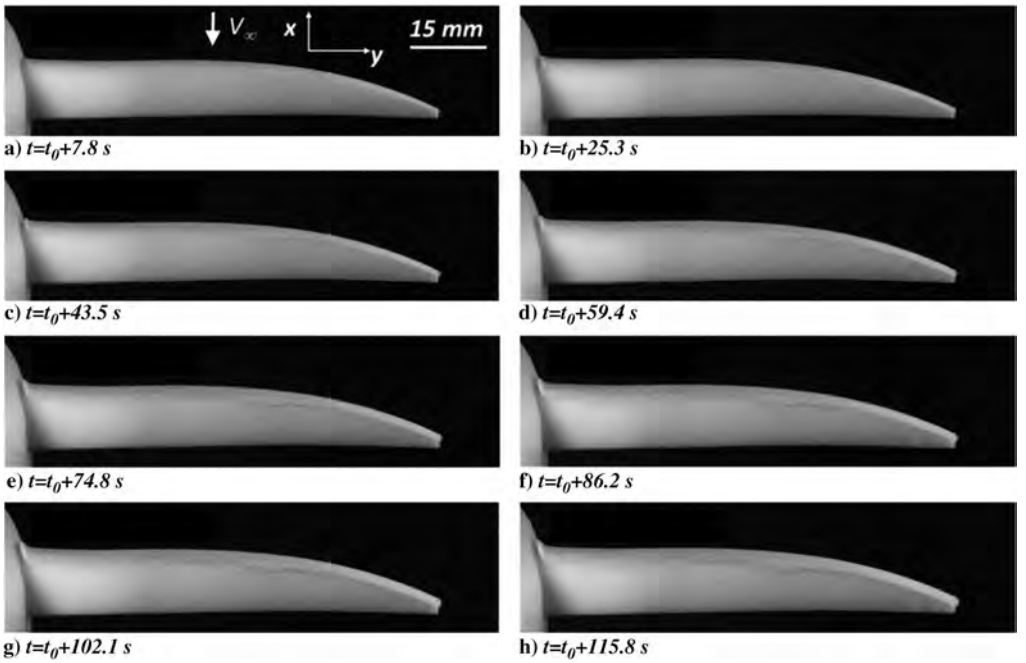

Fig. 4 Time evolution of rime ice accretion process over the rotating propeller blade.

B. Dynamic Icing Process over the Rotating Propeller Blades Under Different Icing Conditions

As described above, a phase-locked imaging technique was used in the present study to provide "frozen" images of the ice features accreted on the rotating propeller blades as a function of time. Figure 4 shows the typical acquired phase-locked images to reveal the dynamic ice accretion process over one of rotating propeller blades under the test condition of freestream airflow velocity $V_\infty = 16$ m/s, LWC $= 1.0$ g/m^3, and the ambient temperature $T_\infty = -15$°C. As the supercooled water droplets carried in the incoming airflow impacted on the blade surfaces under such a cold condition with low humidity, heat transfer process would be conducted very rapidly to dissipate all the latent heat of fusion released during the phase changing of the impinged supercooled water droplets. The ice accretion over the surfaces of the propeller blades was found to exhibit typical rime characteristics (i.e., with milk-white and opaque appearances), similar as those described in the previous study of Hansman and Kirby [31]. As shown clearly in Fig. 4a, because the impinged supercooled water droplets were found to be frozen immediately upon impact, while the surface of the ice accretion was found to be relatively rough due to entrainment of small air bubbles between frozen ice grains, the accreted ice layer was found to conform to the leading edge of the propeller blade well in general. No obvious traces of surface water runback (i.e., formation of rivulet-shaped features as described in [32]) were observed for this test case. The experimental observations also suggest that the formation of rime ice over the surfaces of the rotating blades seems not to be affected noticeably by the centrifugal force due to the immediate freezing of the impinged supercooled water droplets. As the time goes by, with more and more supercooled water droplets impinged and frozen on the surfaces of the rotating propeller blades, the ice layer accreted along the leading edges of the propeller blades was found to become thicker and thicker, as shown clearly in Fig. 4. It should also be noted that, in addition to increasing the thickness of the ice layer along the leading edge of the propeller blade, some noticeable ice feathers were also found to be generated around the midspan of the propeller blades (i.e., at the spanwise location between $0.5R$ and $0.8R$), as revealed clearly in Figs. 4c–4f. Interestingly, the ice feathers were found to grow rapidly outward against the incoming airflow, which would capture more and more supercooled water droplets carried by the incoming airflow. Because of the immediate freezing of the water droplets upon impingement, no water mass would run back to reach to the regions beyond the ice layer accreted along the leading edges of the propeller blades. Therefore, no ice was found to accrete on the surfaces of the propeller blades beyond the direct impact zone of the supercooled water droplets, that is, beyond the region near the leading edge of the propeller blade, as shown clearly in Figs. 4g and 4h.

Figure 5 shows the time sequences of the acquired phase-locked images to reveal the dynamic ice accretion process over the surface of the same propeller blade with speed and LWC level of the incoming airflow being also kept at the same values (i.e., $V_\infty = 16$ m/s and LWC $= 1.0$ g/m^3), but with the ambient temperature being increased to $T_\infty = -5$°C. It can be seen clearly that, instead of forming opaque rime ice as shown in Fig. 4, the ice layer accreted over the blade surface for this test case was found to be semitransparent and have a much smoother appearance, which is similar to the characteristics of typical glaze ice as described in [29,30]. Even though the LWC level in the incoming airflow was still kept at LWC $= 1.0$ g/m^3, due to the much warmer temperature for this test case, the heat transfer (i.e., both heat convection and heat conduction) would not be adequate to remove all the released latent heat of fusion during the solidification of the supercooled water droplets impacted onto the blade surface [33]. As a result, while most of the impacted supercooled water droplets would be froze upon impact, a small portion of the impacted water droplets would still remain in liquid phase, forming a thin water film over the ice-accreting surface of the propeller blade. As driven by the aerodynamic shear force exerted by the boundary-layer airflow around the propeller blade and the centrifugal force associated with the rotation motion of the propeller, the unfrozen water would be transported over the surface of the rotating propeller blade. Because the unfrozen water over the ice-accreting blade surface would easily flow into the voids between the rough ice grains, the ice layer accreted over the propeller blade was found to become much smoother and have a much clearer appearance for this test case, in comparison with rime ice accreted over the blade surface at much colder temperature as shown in Fig. 4. It should also be noted that, due to the effects of the centrifugal force associated with the rotation motion, the unfrozen water accumulated over the blade surface would flow radially from the blade root to blade tip. As a result, needle-shaped ice features were observed at the tip of the propeller blade, as shown clearly in Fig. 5. Because the ice layer accreted over the propeller blade for this test case was still found to be mainly along the leading edge of the propeller blade and conform to

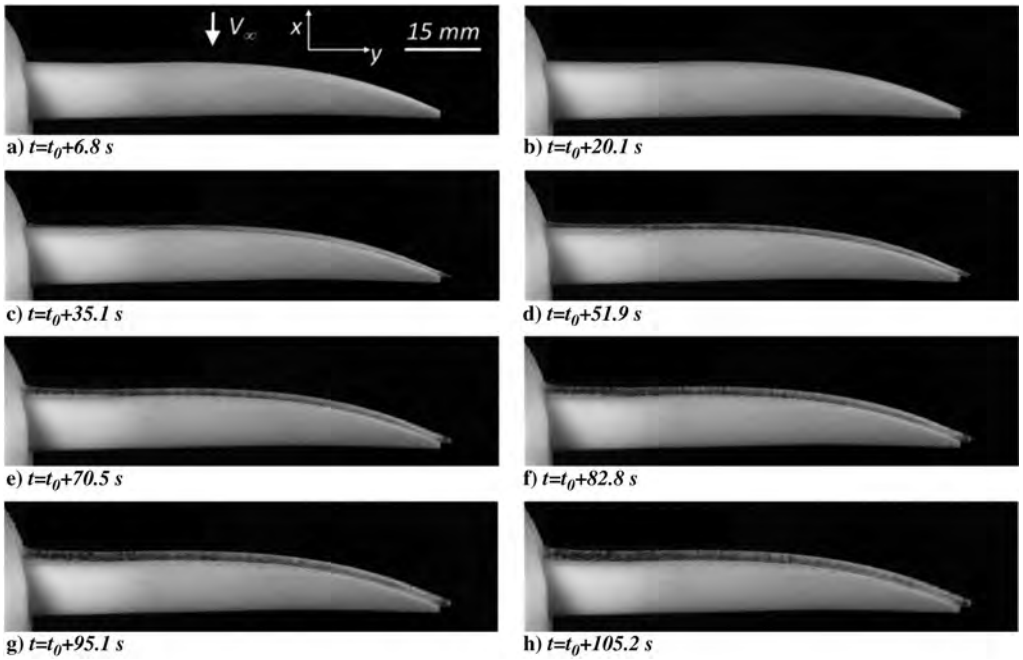

Fig. 5 Time evolution of mixed ice accretion process over the rotating propeller blade.

the airfoil profile of propeller blade well in general, it was also called *mixed* ice accretion [9]; that is, the ice layer accreted over the propeller blade surface was found to have combined characteristics between dry rime ice and wet glaze ice.

Figure 6 shows the time sequence of acquired ice accretion images with the incoming airflow not only being warmer (i.e., $T_\infty = -5°C$), but also much more wetted (i.e., LWC $= 2.0$ g/m^3), in comparison with the rime icing case shown in Fig. 4. Corresponding to the higher LWC level in the incoming airflow for this test case, much more supercooled water droplets would be impinged onto the propeller blade during the same duration of the ice accretion experiment. As described above, due to the much warmer temperature for this test case, the heat transfer process (i.e., both heat convection and heat conduction) would not be fast enough to remove all the released latent heat of fusion during to the solidification of the supercooled water droplets upon impinging onto the blade surface. As a result, only a portion of the supercooled water droplets would be frozen and solidified into ice upon impact, and a large portion of the impinged water mass would still be in liquid, which can flow freely over the surface of the propeller blade. Thus, the ice accretion over the blade surface for this test case was found to be of a typical glaze ice accretion process. As shown clearly in Fig. 6, right after the impingement of the supercooled water droplets onto the blade surface, a water film was found to form rapidly over the ice-accreting surface of the propeller blade. Because of the combined effects of the aerodynamic shear force exerted by the boundary-layer airflow and centrifugal force associated with the rotation motion of the propeller, the impinged water mass was found to be transported quickly away

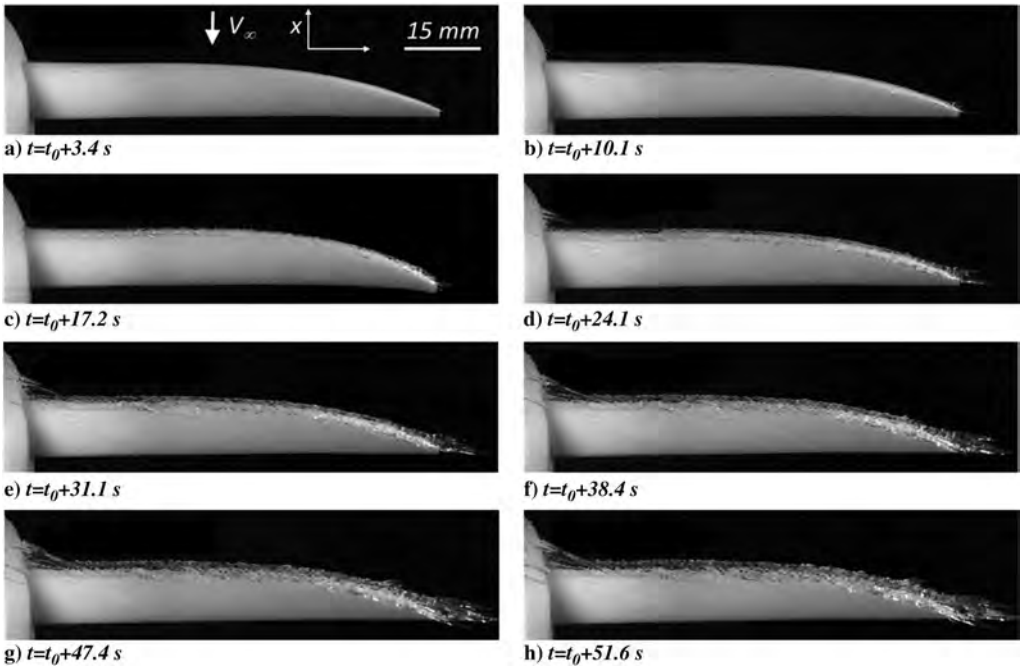

Fig. 6 Time evolution of the glaze ice accretion process over the rotating propeller blade.

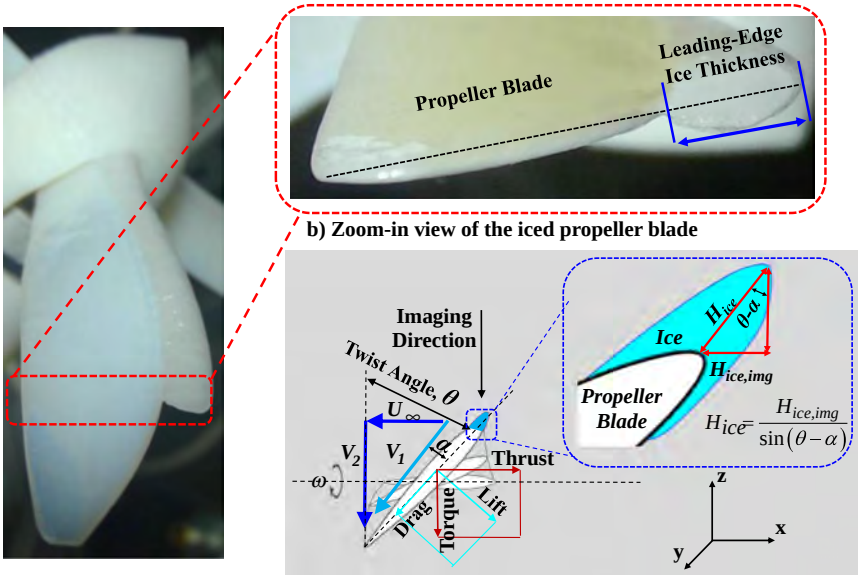

b) Zoom-in view of the iced propeller blade

a) Snapshot of a typical Rime ice accretion

c) Schematic of leading-edge ice accretion on blade element

Fig. 7 A schematic of ice accretion over the leading edge of a propeller blade.

from the direct impingement zone of the supercooled water droplet (i.e., the region near the leading edge of the propeller blade). As driven by the boundary-layer airflow around surface of the propeller blade, the surface water was found to run back along the chordwise direction as rivulets, as reported in Waldman and Hu [32], which would eventually freeze into ice at further downstream beyond the direct impingement zone of the supercooled water droplets. As a result, the ice layer accreted over the surface of the propeller blade was found to extend much further downstream over the blade surface; that is, the coverage of the ice layer over the surface of the blade is much greater for this glaze ice accretion case, in comparison to the rime icing and/or *mixed* icing cases described above. In the meantime, the unfrozen surface water would also be pushed to flow radially from blade root to blade tip due to the effects of the rotation motion of the propeller. Therefore, the ice layer accreted over the outer bound of the propeller blade (i.e., in the region near the blade tip) was found to grow much faster than that at the inner bound of the propeller blade (i.e., in the region close to the blade root). Meanwhile, due to the strong effects of the rotation motion, a portion of the surface water mass was found even to separate from the ice-accreting blade surface to form icicle structures extruding outward into the airflow, as shown clearly in Figs. 6c and 6d. A needle-shaped icicle structure was also found to form at the blade tip due to the effects of the rotation motion.

As the time goes by, with more and more supercooled water droplets impinged onto the propeller blade, much more unfrozen water would be accumulated over the ice-accreting blade surface. The ice accretion process over the blade surface was found to become even more complex due to the very complicated interactions among the multiphase flows (i.e., airflow, impinging water droplets, surface water runback, dynamic solidification, and ice accretion) combined with the effects of the rotation motion. As shown in Figs. 6e and 6f, in addition to the continuous thickness increase of the clear glazy ice layer along the leading edge of the propeller blade, the icicle structures separating from the blade surface were also found to grow rapidly with formation of more complex branches extruding further into the airflow, due to the large amount of water mass being transported toward them as driven by the centrifugal force. The rapid growth of icicle structures sticking out from the surface the conical-shaped propeller spinner can also be observed clearly in the acquired images. As revealed clearly in Figs. 6g and 6h, with more and more water mass impinged onto the ice-accreting surface of the propeller blade, very complex lobster-tail-like ice structures would be formed over the propeller blade. The formation of the irregular lobster-tail-like ice structures was found to significantly degrade the aerodynamic performance of the propeller, which will be further discussed quantitatively in the aerodynamic force measurement section of the presentation.

IV. Further Analysis About the Ice Accretion Process over the Rotating Propeller Blades

As described above, the ice layers accreted along the leading edge of the propeller blade under rime icing or even *mixed* icing conditions were found to conform well to the original profile the propeller blade. Figure 7 shows a zoom-in view of the ice accretion around the leading edge of the propeller blade under such icing conditions. As shown clearly in Fig. 7, the ice layer accreted around the leading edge of the propeller blade has a rather streamlined shape. Such streamlined ice layers could effectively increase the actual airfoil chord length of the rotating propeller blade. In the present study, further efforts were also made to quantify the ice accretion along the leading edge of the propeller blade as a function of time and blade span locations.

The acquired ice accretion images are the maps of the light intensity scattered or reflected from the surfaces of propeller blade, impinged water mass, and accreted ice. By deriving the changes of the intensity maps in the time sequences of the acquired ice accretion images, Waldman and Hu [32] developed an image processing algorithm to extract the feature evolution of dynamic ice accretion process over an airfoil model quantitatively. With the similar image processing procedure as that developed by Waldman and Hu [32], quantitative information about the dynamic ice accretion process along the leading edges of propeller blades can be extracted from the time sequences of the phase-locked images.

Following up the work described in Waldman and Hu [32], the initial reference image of the propeller blade without water or ice over the blade surface was defined as I^0, and the acquired ith image as ice accreted over the propeller blade was defined as I^i. The intensity difference maps for the images of the iced propeller blade, thus, can be derived as

$$I^i_{\text{diff}} = I^i - I^0 \tag{5}$$

By conducting such an image processing procedure, the pixel counts in the intensity difference maps would contain the information about the image changes from the initial state (i.e., propeller blade without water or ice), caused by the presence of water or ice accretion.

Therefore, the advancing front of the ice layer accreted along the leading edges of propeller blades can be identified at every spanwise position y:

$$x^i_{\text{ice}} = \text{first}\left(I^i_{\text{diff}}(x)^2 > \varepsilon\right) \tag{6}$$

where ε was chosen as the six standard deviations of the typical image noise for the present study. The image noise was characterized by calculating the root-mean-square (rms) values of the pixel fluctuations in the blank areas of the images (i.e., areas excluded blade, ice, or water) before ice accretion.

Knowing the initial pixel locations of the blade leading edge, that is, x^i_0, the ice thickness accreted at the leading edge of the propeller can be calculated:

$$H^i_{\text{ice,img}} = K(x^i_{\text{ice}} - x^i_0) \tag{7}$$

where K is the calibration constant in mm/pixel.

In the present study, the propeller blades were designed to have different twist angles along the blade span. The local tangential velocity would also vary due to the increasing radius along the blade spanwise direction. Therefore, the resultant local flow velocity as well as the local stagnation point may vary at the different blade span locations. As described in Özgen and Canıbek [34], because maximum ice accretion would occur at the stagnation line of the airfoil/blades, an estimation of maximum ice accretion over propeller blade can be achieved by finding the stagnation line along the propeller blade based on the local flow direction (i.e., effective angle of attack).

Figure 7c shows a schematic of the ice accretion at the leading edge of a blade element, in which the imaging path is from the top along the vertical direction. It can be seen that the ice thickness captured in the image is a projection of the actual ice thickness in the x–y plane. The relationship between the magnitudes of the imaged ice thickness and the actual ice thickness is

$$H_{\text{ice}} = \frac{H_{\text{ice,img}}}{\sin(\theta - \alpha)} \tag{8}$$

where θ is the local twist angle, and α is the local effective angle of attack, which is defined as

$$\alpha = \theta - \arctan\left(\frac{U}{V_2}\right) \tag{9}$$

where V_2 is the local tangential velocity, which is defined as $V_2 = r \cdot \omega$.

By applying the image process procedure described above, the actual ice thickness accumulated along the leading edge of the propeller blades can be quantitatively extracted. Figure 8 shows the growth of the ice layer accreted along the blade leading edge as a function of the ice accretion time under the icing conditions of $V_\infty = 16$ m/s, $T_\infty = -5°$C, and LWC $= 1.0$ g/m^3. Figure 8a shows the time sequences of the acquired ice accretion images. As indicated by the advancing red line to highlight the moving front surface of ice layer, the thickness of the ice layer accreted along the leading edge of the propeller blade was found to increase continuously as the time goes by. By taking the effects of the blade twist angle (θ) and local effective angle of attack (α) into consideration, the time evolution of the ice layer thickness along the blade leading edge can be extracted quantitatively, which are plotted in Fig. 8b. It is clearly seen that the thickness of the ice layer accreted along the leading edge of the propeller blade increases monotonically from the blade root to tip. This is because the sweeping area for the blade element would increase as a square function of the radius away from the rotation center (i.e., with the minimum at the rotor root and the maximum at the rotor tip), and more water mass would be collected by the blade element located at outer bound of the propeller blade within the same duration of ice accretion process, in comparison with that located at the inner bound of the blade. Furthermore, for the test cases with *mixed or* glaze ice

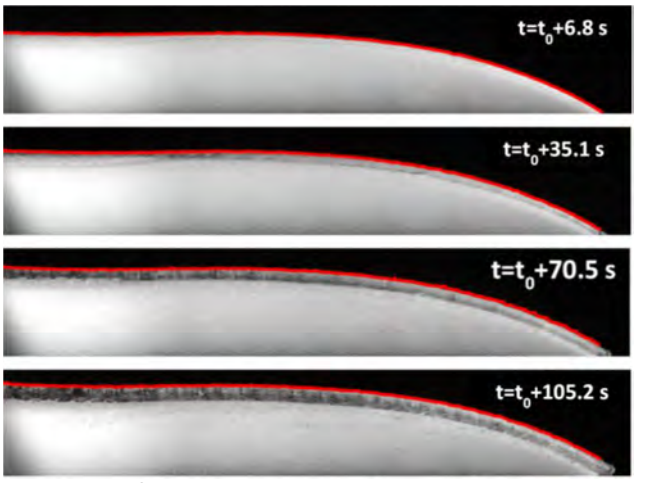

a) Snapshots of leading-edge ice accretion

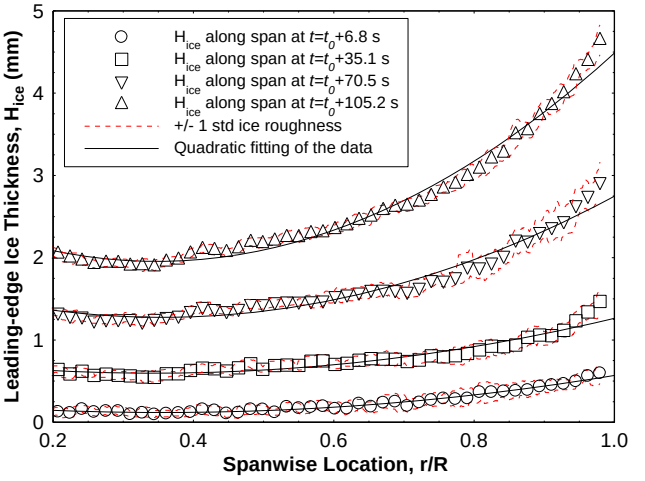

b) Measured leading-edge ice thickness distribution

Fig. 8 Ice accretion along the blade leading edge as a function of the time.

accretion, due to the effects of the centrifugal force associated with the rotation model, surface water transport would also bring additional water mass toward the blade tip, causing more ice accretion at the outer bound of the rotating propeller blade. The findings were found to agree well with the observations reported in the previous studies of Fortin and Perron [25] and Lamraoui et al. [24] to investigate rotorcraft icing phenomena.

More specifically, as shown in Fig. 8a, for the *mixed* ice accretion case with the test conditions of $V_\infty = 16$ m/s, $T_\infty = -5°$C, and LWC $= 1.0$ g/m^3, the ice layer thickness at the leading edge of the blade tip was found to exceed $H = 4.5$ mm in about 105 s after starting the ice accretion process, whereas the ice thickness near the blade root (i.e., $r/R = 0.2$) was found to be only about $H \approx 2.0$ mm. In comparison to the original chord lengths of the propeller blade (i.e., $c_{\text{root}} = 11.6$ mm and $c_{\text{tip}} = 3.4$ mm), the changes in the effective chord lengths of the propeller blade due to the ice accretion were found to be very significant, especially at the outer bound of the propeller blade (i.e., increased by 130% at the blade tip in 105 s after starting the ice accretion process). It should also be noted that the dotted lines given in Fig. 8b indicate the ± 1 standard deviation (STD) variations of the measured ice thickness about the mean thickness value of the ice layer accreted along the blade leading edge. It can be seen clearly that, as the time goes by, while the thickness of ice layer accreted along the leading edge of the propeller blade was found to increase rapidly, the surface roughness of the ice layer was also found to increase greatly. Similar findings were also reported in the previous icing study of Waldman and Hu [32] to examine the dynamic ice accretion process over a two-dimensional airfoil/wing model.

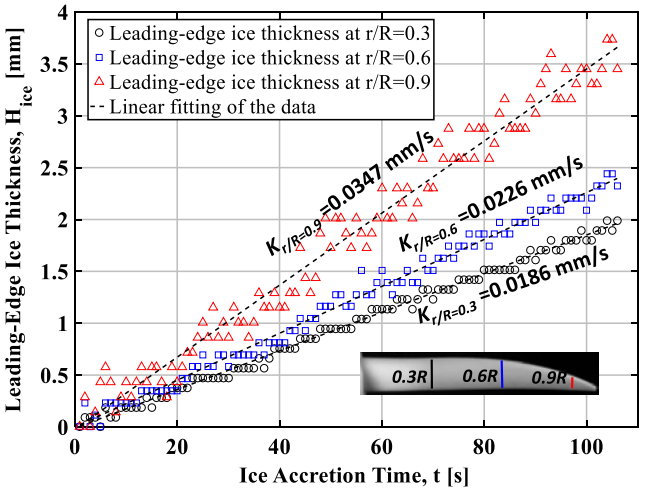

Fig. 9 Time histories of leading-edge ice thickness at three typical blade span locations.

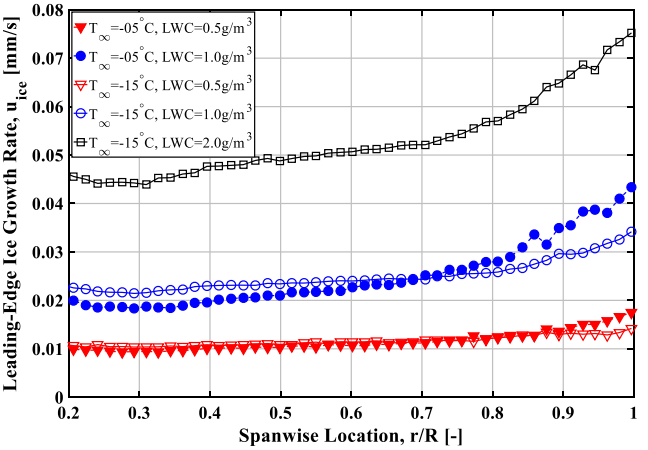

Fig. 10 Measured ice growth rates under different icing conditions.

It should also be noted that the roughness of the ice layer accreted in the outer regions of the propeller blade, especially in the regions near the blade tip, was found to be much greater than that near the root of the propeller blade, due to the stronger effects of centrifugal force in the outer bound region. Because the accreted ice mass along the radial direction of the propeller blade is expected to be in proportional to the sweeping area of each rotor blade segment (i.e., in a square function of the radius), the measured ice thickness data were fitted with quadratic curves, as shown in Fig. 8b.

Figure 9 shows the time histories of the measured thickness of the ice layer accreted at three typical span locations (i.e., at $r/R = 0.3, 0.6$, and 0.9), which can be used to reveal the characteristics of the dynamic ice accretion process over the propeller blade surface more quantitatively. It can be seen clearly that, while the ice layer accreted along the leading edge of the propeller blade was found to increase continuously, the relationships between the ice layer thickness at different spanwise locations and the ice accretion time were all found to be fitted well by using linear functions. As described above, corresponding to the larger sweeping area for a blade element at the outer bound of the propeller blade, the ice layer accreted at the outer bound of the propeller blade was found to increase much faster, in comparison with that at the inner bound of the propeller blade. As shown quantitatively in Fig. 9, the ice growth rate at the outer bound of the propeller blade (e.g., at the spanwise location of $r/R = 0.9$) was found to have a very rapid increasing slope of $K_{r/R=0.9} = 0.0347$ mm/s, which is almost twice greater than that at the inner bound of $r/R = 0.3$ (i.e., the slope of the fitted line was found to be only $K_{r/R=0.3} = 0.0186$ mm/s). It can also be seen that, corresponding to the much roughened ice structures formed at the outer region of propeller blade, the scattering range of the measured ice thickness data at the outer bound of propeller blade was found to be much wider than those in the inner region of the propeller blade (e.g., at the spanwise location of $r/R = 0.3$).

By extracting the linear regression slopes of the lines fitted to the measured ice thickness data as those shown in Fig. 9, the ice growth rates along the spanwise direction of the propeller blade under different icing conditions can be determined, which are plotted in Fig. 10. It can be clearly seen that, at a constant ambient temperature (i.e., at either $T_\infty = -15°C$ or $T_\infty = -5°C$), the growth rate of the ice layer accreted over the blade surface was found to increase proportionally to the LWC level of the incoming airflow. More specifically, for the test cases with same temperature of $T_\infty = -15°C$, the growth rate of the ice layer accreted over the propeller blade was found to increase almost by a factor of 4.0 as the LWC level of the incoming airflow was increased from LWC = 0.5 g/m^3 to LWC = 2.0 g/m^3. Because the ice accretion process under relatively colder conditions (i.e., $T_\infty = -15°C$) would be a typical rime icing process, as suggested by Anderson [35], the ice accumulation parameter, A_c, can be defined as

$$A_c = \frac{\text{LWC} \cdot V_\infty \cdot \tau}{d \cdot \rho_i} \tag{10}$$

where τ is the duration of the ice accretion process, d is the twice the leading-edge radius of airfoil, and ρ_i is the ice density, the time derivative of the ice accumulation parameter can be used to estimate the growth rate of the ice layer accreted near the leading edge of the propeller blade, that is,

$$\frac{dA_c}{d\tau} = \frac{\text{LWC} \cdot V_\infty}{d \cdot \rho_i} \tag{11}$$

It is obvious that, as the velocity of the incoming airflow, V_∞, is kept at a constant, the growth rate of ice accretion would be proportional linearly to the LWC level of the incoming airflow, which was confirmed by the measurement results given in Fig. 10. It is also revealed clearly that, when the LWC level of the incoming airflow was kept at the same, the ice accretion over the surface of the propeller blade was found to vary noticeably as the ambient temperature was changed from $T_\infty = -15°C$ to $T_\infty = -5°C$. More specifically, in comparison to those test cases with colder temperature (i.e., $T_\infty = -15°C$), while the ice growth rates at the inner bound of the propeller blade were found to be slightly slower for the cases with relatively warmer temperature (i.e., $T_\infty = -5°C$), a completely opposite trend was observed for the ice accretion at the outer bound of the propeller blade. This can be explained by the facts that, because the ice accretion process at relatively warmer temperatures (e.g., $T_\infty = -5°C$) would most likely glaze ice accretion, some of the impinged supercooled water droplets would not be frozen immediately upon impact. Because of the effects of the centrifugal force associated with the rotation motion, the surface water would be transported from the root region toward the tip of the rotating blade. As a result, in comparison with the test cases with much colder ambient temperature (i.e., most likely rime ice accretion process at $T_\infty = -15°C$), while less ice accretion was found in the inner region of the propeller blade for the glaze icing cases at relatively warmer temperatures (i.e., $T_\infty = -5°C$), more ice accretion would be accreted at the outer bound of the rotating propeller blade, as shown quantitatively in Fig. 10.

A. Thrust Characteristics of the Propeller Model Under Different Icing Conditions

As described above, a high-sensitive JR3 load cell (Model 30E12A-I40) was used in the present study to achieve time-resolved measurements of aerodynamic loads acting on the propeller model under different icing conditions. While similar features can also be revealed by other components of the aerodynamic forces and moments, only the measured thrust fore data are given in the present study for analysis for conciseness.

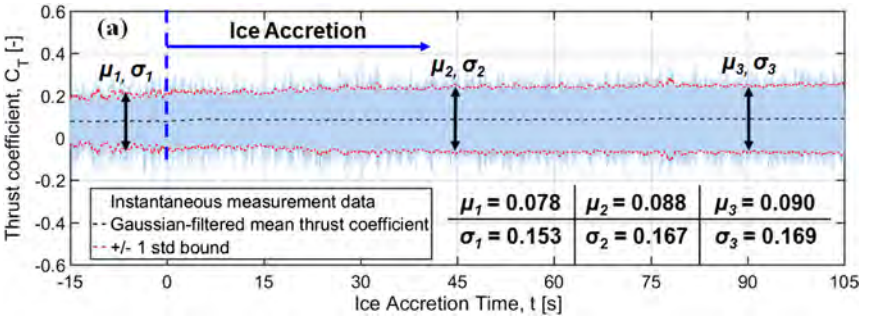

Fig. 11 Measured thrust coefficient of the propeller model during the rime ice accretion process.

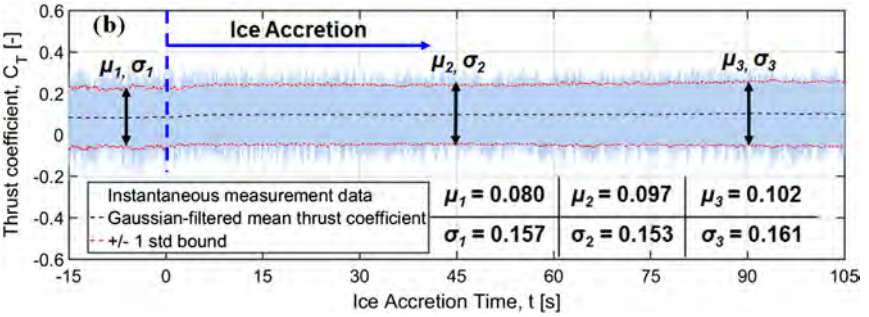

Fig. 12 Measured thrust coefficient of the propeller model during the mixed ice accretion process.

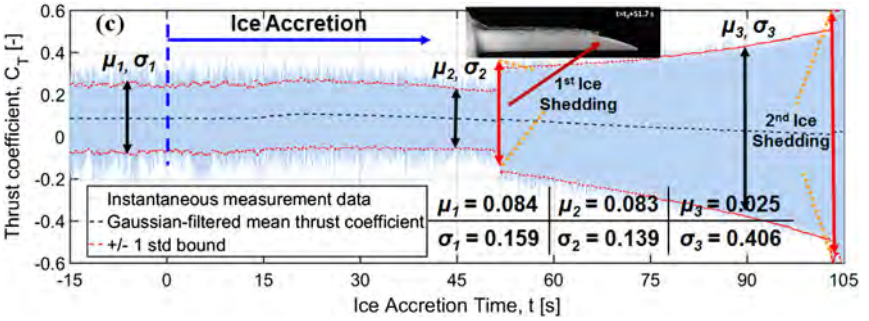

Fig. 13 Measured thrust coefficient of the propeller model during the glaze ice accretion process.

In the present study, the aerodynamic force measurements were first sampled for 15 s before switching on the water spray system to start the ice accretion process, which will be used as the baseline to evaluate the effects of ice accretion on the thrust generation characteristics of the UAS propeller. Then, the aerodynamic force data were acquired continuously for about 120 s with the water spray system being switched on to enable ice accreting dynamically over the rotating propeller blades. Figures 11–13 give the examples of the measured thrust force data, in terms of the instantaneous thrust coefficient, C_T, with the propeller model operated under three typical icing conditions described above. The Gaussian-filtered mean values and the ± 1.0 standard deviation (STD) bounds of the instantaneous measurement results were also given in the plot for comparison. The mean (μ) and standard deviation (σ) of the measured thrust coefficient at three typical moments, that is, before ice accretion (μ_1, σ_1), after 45 s of ice accretion (μ_2, σ_2), and after 90 s of ice accretion (μ_3, σ_3), were also calculated and given in the plot.

Figure 11 shows the measured thrust coefficient of the propeller model during the rime ice accretion process with the test conditions of $V_\infty = 16$ m/s, $T_\infty = -15°$C, and LWC $= 1.0$ g/m^3. In comparison with the measurement results before turning on the water spray system (i.e., without ice accretion), while the measured thrust coefficient data were found to have slightly higher fluctuation amplitude (i.e., as indicated by the slightly wider ± 1.0 STD bounds) due to the dynamic ice accretion, the mean value of the thrust coefficient was also found to increase slightly as the ice started to accrete over the rotating propeller blades for this test case. As described above, the ice accretion over the surfaces of the rotating propeller blades for this test case is a typical rime icing process. The accreted rime ice at the leading edges of the propeller blades would closely follow the original airfoil profiles of the propeller blades. As the time goes on, the rime ice layer accreted along the leading edges of the propeller blades was found to become thicker and thicker, as shown clearly in Fig. 4, which actually effectively extended the chord length of the propeller blades. As a result, a greater lift force would be generated by the propeller model due to the rime ice accretion. In the meantime, the aerodynamic drag force acting on the propeller would also be increased due to the larger effective area of the iced blades and the rougher surfaces of the rotating propeller blades associated with the dynamic ice accretion. Therefore, the slight increase of the mean value of the thrust coefficient (i.e., ~15% increase in mean thrust after 90 s of the rime accretion, as shown in Fig. 11) is believed to be caused by the increased effective chord length of the propeller blades associated with the rime ice accretion. As reported in the previous study of Ueno and Farzaneh [8], ice accretion process is highly unsteady (sometimes even becoming random). Even for the propeller blades with exactly the same shapes and dimensions, the total mass of the accreted

ice and resultant ice shape may vary in the different trials even under the same icing conditions. The slight increase of the force fluctuation amplitude (i.e., ∼10% increase in standard deviation value of the fluctuation amplitude after 90 s of the rime accretion, as shown in Fig. 11) for the rime ice accretion case is believe to be caused by the unsymmetrical ice accretion over the three propeller blades due to the uncertainties in ice accretion process.

Figure 12 gives the time history of the measured instantaneous thrust coefficients of the UAS propeller model during the *mixed* ice accretion process with a warmer ambient temperature (i.e., $T_\infty = -5°C$). As described above, the ice layer accreted over the propeller blade for this test case was found to concentrate mainly along the leading edge of the propeller blade and conform to the airfoil profile of propeller blade well in general. In comparison with those with rime ice accretion over the rotating propeller blades as described above, very similar characteristics of the thrust force generated by the propeller model were observed during the *mixed* ice accretion process. While the mean value of the thrust force generated by the propeller model was found to increase slightly as ice began to build up over the blade surfaces (i.e., ∼13% increase in mean thrust after 90 s of the *mixed* accretion, as shown in Fig. 12), fluctuation amplitudes of the instantaneous thrust forces were found to stay almost the same as those without ice accretion, as indicated by the almost unchanged width of the ±1 STD bounds during the mixed ice-accreting process (i.e., within ∼2.5% of variation in standard deviation value of the fluctuation amplitude, as shown in Fig. 12). The slight increase of the mean value of the thrust coefficients is believed to be caused by the continuous growth of the effective chord length of the propeller blades due to the ice accretion along the leading edges of the propeller blades. Because the ice layer accreted over the propeller blade surface was found to become much smoother for this *mixed* ice accretion case in comparison with the rime ice accretion case described above, the relatively constant fluctuation of the thrust force is believed to be closely related to the smaller aerodynamic drag force acting on the smoother ice-accreting blade surface and the increased moment of inertia of the rotating propeller model as more and more ice accumulated over the outer bound of the propeller blades under such a *mixed* ice accretion process.

Figure 13 shows the time history of the measured thrust force generated by the propeller model with the test conditions of $V_\infty = 16$ m/s, $T_\infty = -5°C$, and LWC $= 2.0$ g/m^3. As described above, the ice accretion over the propeller blades was found to become typical glaze ice accretion process with evident surface water transport and irregular icicle structures formed on the surfaces of the propeller blades, as shown clearly in Fig. 6. It is clearly seen that, as the ice layer began to build up on the surfaces of the propeller blades, a slight increase of the mean thrust value was found at the initial stage of the ice accretion process (i.e., before $t = 30$ s), while the fluctuation amplitude of the thrust force was found to be almost unchanged, which is similar as *mixed* ice accretion process described above. As more and more supercooled water droplets impinged onto the surfaces of the propeller blades (i.e., $t > 30$ s), due to the combined effects of the aerodynamic shear stress exerted by the boundary-layer airflow around the propeller blade and the centrifugal force associated with the rotation motion, more water mass would be transported toward the outer bounds of the propeller blades and froze into very complex lobster-tail-like icicle structures, as shown clearly in Fig. 6. The formation of the complex lobster-tail-like icicle structures over the surfaces of the rotating propeller blades would degrade the aerodynamic performance of the propeller blade greatly. As a result, the thrust force generated by the propeller model was found to start to decrease, while the fluctuation amplitude of the instantaneous thrust force was also found to become smaller due to the rapid increase of the moment of inertia for the propeller model as more and more ice accumulated at the outer bound of the propeller blades.

As the time goes by, with more and more supercooled water droplets impinging onto the blade surfaces, the lobster-tail-like icicle structures extruding out from the ice-accreting surfaces of the propeller blades were found to grow continuously. The centrifugal forces acting on the complex lobster-tail-like ice structures would also become greater and greater due to the continuous mass increase of the accreted ice. Once the centrifugal force overcame the adhesion force between the accreted ice and the surfaces of the propeller blades, ice shedding would occur, as shown clearly in Fig. 13. The sudden ice shedding was found to cause a dramatic fluctuation of the forces acting on the propeller model, due to the unbalance of the mass distribution for the three-blade propeller, as can be seen at $t = 51.7$ s as indicated in Fig. 13. While the glaze ice accretion process would occur continuously over the surfaces of the rotating propeller blades, the unbalance mass distribution among the three rotor blades would cause significant increase of the fluctuation amplitude of the aerodynamic forces acting on the propeller model (i.e., the STD value of the fluctuation amplitude was found to increase 250% at 90 s after starting the glaze ice accretion process, as shown in Fig. 13). Meanwhile, the mean thrust value was also found to keep on decreasing due to the further degraded aerodynamic performance of the propeller associated with the rapid growth of the irregular icicle structures over the surfaces of the propeller blades (i.e., over ∼70% decrease in mean thrust after 90 s of the glaze ice accretion). As shown clearly in Fig. 13, a second ice shedding was found to occur at the time instance of $t = 102.5$ s, which would further downgrade the aerodynamic performance of the propeller. The larger fluctuations in the thrust force generation would indicate much more troublesome in UAS flight control as well as significant fatigue loads acting on the propellers when UAS is operated in glaze icing conditions. Such quantitative force measurements under different icing conditions highlight the great importance of taking the icing conditions into account for more efficient and safer UAS operations in cold weather.

B. Characteristics of the Power Consumption by the Propeller Model Under Different Icing Conditions

In addition to the measuring the aerodynamic forces acting on the propeller model, the power inputs required to drive the propeller model to rotate at a constant rotation speed (i.e., $n = 3000$ rpm) under different icing conditions were also monitored in the present study. Figure 14 shows the required power inputs to drive the propeller model as a function of time under the three typical icing conditions described above. The required power inputs under different icing conditions were normalized by their corresponding baseline values without any ice accretion over the propeller blades, that is, $Cp_{\text{ice}}/Cp_{\text{no-ice}}$, for quantitative comparison.

It is clearly seen that, for the test case with rime ice accretion over the propeller blades (i.e., with the ambient temperature of $T_\infty = -15°C$ and LWC $= 1.0$ g/m^3), the required power input was found to increase slightly as ice began to build up on the surfaces of the rotating propeller blades. As mentioned above, the rime ice accretion was found to concentrate mainly along the leading edges of the propeller blades with noticeable surface roughness. A greater aerodynamic drag is expected to act on the propeller model due to the increased surface roughness associated with the rime ice accretion. Meanwhile, the ice accretion would also increase the total mass of the rotating propeller. Therefore, the required power input was found to increase gradually in order to keep the ice-accreting propeller rotating at the same rotational speed, as revealed quantitatively with the black dashed line given in Fig. 14. More specifically, about 20% more power input would be required after 90 s to start the ice accretion experiment for this test case.

A similar power input performance was also observed for the *mixed* ice accretion case with the ambient temperature of $T_\infty = -5°C$ and LWC $= 1.0$ g/m^3, which was indicated as the blue broken line given in Fig. 14. As mentioned above, because a small portion of the supercooled water droplets would not be frozen immediately upon impact for this test case, the unfrozen water mass would be transported over the surfaces of the rotating propeller blades, due to the combined effects of aerodynamic shear stress and centrifugal force. It would cause more ice accretion over the outer bounds of the rotation propeller blades as well as formation of needle-shaped ice features extruding out from the blade tips as shown in Fig. 5. In comparison to the rime ice accretion case as described above, a slightly greater power input (i.e., 30% more power input after 90 s of ice accretion process as shown in Fig. 14) was required in order to drive the propeller to rotate at the constant rotation speed of

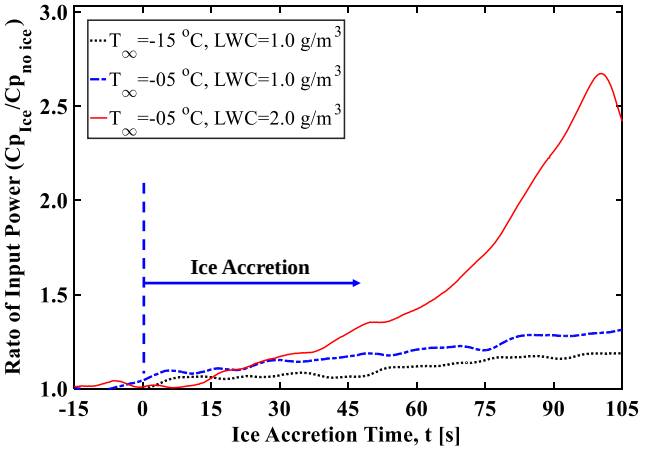

Fig. 14 The required power inputs to drive the propeller model under different icing conditions.

$n = 3000$ rpm during the *mixed* ice accretion process. Such a slight increase in the required power input is believed to be closely related to the increased aerodynamic drag owing to the surface water transport and greater ice roughness formation at outer bounds of the propeller blade (i.e., the formation of needle-shaped ice features as shown in Fig. 5), as well as the increased moment of inertia associated with the faster ice accretion at the outer bounds of the rotating propeller blades.

As indicated clearly in the red solid-line given in Fig. 14, for the test case of typical glaze icing process with a much wetter incoming airflow and warmer ambient temperature (i.e., $T_\infty = -5°C$; LWC $= 2.0$ g/m^3), the required power input was found to increase dramatically in order to drive the propeller model to rotate at the same rotation speed of $n = 3000$ rpm. As described above, because a much larger amount of the impinged supercooled water droplets would be still in liquid upon impact for this test case, the unfrozen water mass would run back over the surfaces of the propeller blades, as driven jointly by both the aerodynamic shear stress and centrifugal force. Very complex ice structures were found to be generated over the surfaces of rotating propeller blades and propeller spinner for this test case (e.g., the formation of lobster-tail-like icicle structures at the blade tips, as shown in Fig. 6). Because the shapes of the accreted ice structures over surfaces of the propeller blades and spinner were highly irregular, they would drastically degrade the aerodynamic performance of the propeller model. As a result, the aerodynamic drag acting on the propeller and the total mass of the rotating propeller would increase significantly, in comparison with those of the baseline value without any ice accretion. Therefore, a much greater power input was required in order to keep the propeller rotating at the same rotation speed (i.e., up to about 250% more power input is required at 90 s after starting the glaze ice accretion process, as shown in Fig. 14). It can also be seen that, as large chucks of accreted ice were shed from the rotating propeller blades, a decrease of the required power input was also observed due to the sudden decrease of the rotating mass, as shown clearly in Fig. 14 at the instant time of $t = 105$ s. In summary, as shown quantitatively in Fig. 14, despite of different accreted ice types, the required power inputs to drive the propeller model were all found to increase greatly due to the ice accretion over the propeller blades. Dramatically greater power consumptions were found for the propeller operating under glaze icing conditions. The greater power consumptions for UAS propellers under icing conditions would indicate that a shorter flight duration or more powerful batteries would be expected for UAS operation under icing conditions.

V. Conclusions

In the present study, a comprehensive experimental study was conducted to investigate the transient ice accretion process over the surfaces of a rotating UAS propeller. The experimental study was performed in the Icing Research Tunnel of Iowa State University (i.e., ISU-IRT) with a scaled UAS propeller model operated under a variety of icing conditions (i.e., ranged from dry rime to wet glaze ice accretion). A phase-locked imaging technique was used to reveal the details of the transient ice accretion process over the surfaces of the rotating propeller blades. The dynamic thrust forces generated by the propeller model and the required power input to drive the propeller to rotate at a constant rotation speed were also measured simultaneously during the transient ice accretion process. Based on such temporally synchronized and spatially resolved measurements, the effects of the dynamic ice accretion process on the characteristics of the dynamic thrust force generated by the propeller model and the required power input to drive the propeller were examined in great details.

It was found that, as the propeller model was operated under rime icing conditions, the ice accretion conformed to the airfoil profiles of the propeller blades well in general, and the rotation motion of the propeller was found to have no noticeable effects on the ice accretion process over the surfaces of the propeller blades. While under glaze icing conditions, due to the combined effects of the aerodynamic shear force exerted by the boundary-layer airflow and centrifugal force associated with the rotation motion of the propeller, the unfrozen water mass was found to be transported from the blade root regions toward blade tips and formed very complex icicles, or even lobster-tail-like ice structures, which would significantly degrade the aerodynamic performance of the propeller. Corresponding to the larger sweeping area at the outer bound of the propeller blade and the radial surface water transportation over the blade surface due to the effects of centrifugal forces associated with the rotation motion, the thickness of the ice layers accreted at the outer bound of the propeller blades was found to increase much faster than that in the inner region of the propeller blades.

In comparison with the baseline case without ice accretion, the propeller model with rime ice accretion over the propeller blades was found to be able to generate slightly higher thrust force (i.e., ~15% greater in the mean thrust value after 90 s of the rime accretion process) due to the increased effective chord length of the propeller blades associated with the well conformed rime ice accretion along the leading edges of the propeller blades. However, fluctuation amplitudes of the instantaneous thrust forces generated by the iced propeller model were also found to increase slightly (i.e., ~10% increase in the standard deviation value of the instantaneous thrust forces after 90 s of the rime ice accretion) due to the combined effects of the rather rough surface of the iced propeller blades and the random ice accretion over the propeller blades. The characteristics of the thrust generation for the propeller model were found to become much more complicated under glaze ice accretion conditions. While the propeller model was found to generate a slight greater thrust force at the initial stage of the glaze ice accretion process, the aerodynamic performance of the propeller was found to degrade significantly at later stage of the glaze ice accretion process with the formation of very complicated icicle structures, for example, lobster-tail-like ice structures, extruding out from the ice-accreting surfaces of the propeller blades. The complex icicle structures were also found to shed suddenly from the rotating propeller blades, which would cause dramatic fluctuations for the instantaneous thrust forces generated by the propeller model. More specifically, while the mean value of thrust force generated by the propeller model was found to decrease ~70% at 90 s after the starting of the glaze ice accretion process, the fluctuation amplitudes of the instantaneous thrust forces were found to increase 255% due to glaze ice accretion. The much lower mean thrust value and the significantly increased fluctuations in the thrust force generation due to ice accretion would indicate much more troublesome in UAS flight control as well as significant fatigue loads acting on the propeller blades when the UAS was operated under glaze icing conditions.

The power consumption measurements revealed clearly that, despite of different types of ice accretion over the propeller blades, the propeller model was always found to consume more power

inputs under icing conditions. More specifically, in comparison with those without ice accretion, while ∼20% more power inputs were required to drive the propeller model at 90 s after starting the rime ice accretion process, up to about 250% more power inputs was found to be required under the glaze ice accretion conditions. The greater power consumptions for UAS propellers under icing conditions would indicate that a shorter UAS flight duration or more powerful batteries would be expected for UAS operation under icing conditions.

Acknowledgments

The authors thank Dr. Rye Waldman, Mr. James Benson, and Mr. Andrew Jordan of Iowa State University for their help in operating ISU Icing Research Tunnel (ISU-IRT) Facility. The research work is partially supported by Iowa Space Grant Consortium (ISGC) Base Program for Aircraft Icing Studies, National Aeronautics and Space Administration (NASA) with the grant number of NNX16AN21A, and National Science Foundation (NSF) under award numbers of CBET-1064196 and CBET-1435590.

References

[1] Pajares, G., "Overview and Current Status of Remote Sensing Applications Based on Unmanned Aerial Vehicles (UAVs)," *Photogrammetric Engineering & Remote Sensing*, Vol. 81, No. 4, 2015, pp. 281–330. doi:10.14358/PERS.81.4.281

[2] Dong, W., Zhu, J., Zheng, M., Lei, G. L., and Zhou, Z. X., "Experimental Study on Icing and Anti-Icing Characteristics of Engine Inlet Guide Vanes," *Journal of Propulsion and Power*, Vol. 31, No. 5, 2015, pp. 1330–1337. doi:10.2514/1.B35679

[3] Habashi, W. G., Veillard, X., and Baruzzi, G. S., "Icing Simulation in Multistage Jet Engines," *Journal of Propulsion and Power*, Vol. 27, No. 6, 2011, pp. 1231–1237. doi:10.2514/1.B34060

[4] Dong, W., Zheng, M., Zhu, J., Lei, G., and Zhao, Q., "Experimental Investigation on Anti-Icing Performance of an Engine Inlet Strut," *Journal of Propulsion and Power*, Vol. 33, No. 2, 2017, pp. 379–386. doi:10.2514/1.B36067

[5] Liu, Y., Bond, L. J., and Hu, H., "Ultrasonic-Attenuation-Based Technique for Ice Characterization Pertinent to Aircraft Icing Phenomena," *AIAA Journal*, Vol. 55, No. 5, 2017, pp. 1602–1609. doi:10.2514/1.J055500

[6] Campbell, S. E., Broeren, A. P., and Bragg, M. B., "Sensitivity of Aircraft Performance to Icing Parameter Variations," *Journal of Aircraft*, Vol. 44, No. 5, 2007, pp. 1758–1760. doi:10.2514/1.32355

[7] Bragg, M., Gregorek, G., and Lee, J., "Airfoil Aerodynamics in Icing Conditions," *Journal of Aircraft*, Vol. 23, No. 1, 1986, pp. 76–81. doi:10.2514/3.45269

[8] Ueno, K., and Farzaneh, M., "Linear Stability Analysis of Ice Growth Under Supercooled Water Film Driven by a Laminar Airflow," *Physics of Fluids*, Vol. 23, No. 4, 2011, Paper 42103. doi:10.1063/1.3575605

[9] Fortin, G., Laforte, J.-L., and Ilinca, A., "Heat and Mass Transfer During Ice Accretion on Aircraft Wings with an Improved Roughness Model," *International Journal of Thermal Sciences*, Vol. 45, No. 6, 2006, pp. 595–606. doi:10.1016/j.ijthermalsci.2005.07.006

[10] Liu, Y., Chen, W.-L., Bond, L. J., and Hu, H., "An Experimental Study on the Characteristics of Wind-Driven Surface Water Film Flows by Using a Multi-Transducer Ultrasonic Pulse-Echo Technique," *Physics of Fluids*, Vol. 29, No. 1, 2017, Paper 12102. doi:10.1063/1.4973398

[11] Lee, S., and Loth, E., "Simulation of Icing on a Cascade of Stator Blades," *Journal of Propulsion and Power*, Vol. 24, No. 6, 2008, pp. 1309–1316. doi:10.2514/1.37810

[12] Beaugendre, H., Morency, F., and Habashi, W. G., "FENSAP-ICE's Three-Dimensional In-Flight Ice Accretion Module: ICE3D," *Journal of Aircraft*, Vol. 40, No. 2, 2003, pp. 239–247. doi:10.2514/2.3113

[13] Botura, G., and Fahrner, A., "Icing Detection System—Conception, Development, Testing and Applicability to UAVs," AIAA Paper 2003-6637, 2003. doi:10.2514/6.2003-6637

[14] Szilder, K., and McIlwain, S., "In-Flight Icing of UAVs—The Influence of Flight Speed Coupled with Chord Size," *Canadian Aeronautics and Space Journal*, Vol. 58, No. 2, 2012, pp. 83–94. doi:10.5589/q12-007

[15] Zhang, B., Tang, L., and Roemer, M., "Probabilistic Weather Forecasting Analysis for Unmanned Aerial Vehicle Path Planning," *Journal of Guidance, Control, and Dynamics*, Vol. 37, No. 1, 2014, pp. 309–312. doi:10.2514/1.61651

[16] Siquig, R., "Impact of Icing on Unmanned Aerial Vehicle (UAV) Operations," Tech. Rept. PR 90:015:442, Naval Oceanographic and Atmospheric Research Lab., Monterey, CA, 1990.

[17] Bottyán, Z., "In-Flight Icing Characteristics of Unmanned Aerial Vehicles During Special Atmospheric Condition over the Carpathian-Basin," *Acta Geographica Debrecina: Landscape & Environment*, Vol. 7, No. 2, 2013, pp. 74–80.

[18] Armanini, S. F., Polak, M., Gautrey, J. E., Lucas, A., and Whidborne, J. F., "Decision-Making for Unmanned Aerial Vehicle Operation in Icing Conditions," *CEAS Aeronautical Journal*, Vol. 7, No. 4, 2016, pp. 663–675. doi:10.1007/s13272-016-0215-2

[19] Sørensen, K. L., Helland, A. S., and Johansen, T. A., "Carbon Nanomaterial-Based Wing Temperature Control System for In-Flight Anti-Icing and De-Icing of Unmanned Aerial Vehicles," *2015 IEEE Aerospace Conference*, IEEE Paper 15215885, Piscataway, NJ, 2015, pp. 1–6.

[20] Coffman, H. J., "Helicopter Rotor Icing Protection Methods," *Journal of the American Helicopter Society*, Vol. 32, No. 2, 1987, pp. 34–39. doi:10.4050/JAHS.32.34

[21] Overmeyer, A., Palacios, J., and Smith, E., "Ultrasonic De-Icing Bondline Design and Rotor Ice Testing," *AIAA Journal*, Vol. 51, No. 12, 2013, pp. 2965–2976. doi:10.2514/1.J052601

[22] Palacios, J. L., Han, Y., Brouwers, E. W., and Smith, E. C., "Icing Environment Rotor Test Stand Liquid Water Content Measurement Procedures and Ice Shape Correlation," *Journal of the American Helicopter Society*, Vol. 57, No. 2, 2012, pp. 29–40. doi:10.4050/JAHS.57.022006

[23] Palacios, J., Smith, E., Rose, J., and Royer, R., "Ultrasonic De-Icing of Wind-Tunnel Impact Icing," *Journal of Aircraft*, Vol. 48, No. 3, 2011, pp. 1020–1027. doi:10.2514/1.C031201

[24] Lamraoui, F., Fortin, G., Benoit, R., Perron, J., and Masson, C., "Atmospheric Icing Impact on Wind Turbine Production," *Cold Regions Science and Technology*, Vol. 100, April 2014, pp. 36–49. doi:10.1016/j.coldregions.2013.12.008

[25] Fortin, G., and Perron, J., "Spinning Rotor Blade Tests in Icing Wind Tunnel," AIAA Paper 2009-4260, 2009, doi:10.2514/6.2009-4260

[26] Han, Y., Palacios, J., and Schmitz, S., "Scaled Ice Accretion Experiments on a Rotating Wind Turbine Blade," *Journal of Wind Engineering and Industrial Aerodynamics*, Vol. 109, Oct. 2012, pp. 55–67. doi:10.1016/j.jweia.2012.06.001

[27] Chen, T. Y., and Liou, L. R., "Blockage Corrections in Wind Tunnel Tests of Small Horizontal-Axis Wind Turbines," *Experimental Thermal and Fluid Science*, Vol. 35, No. 3, 2011, pp. 565–569. doi:10.1016/j.expthermflusci.2010.12.005

[28] Brandt, J., and Selig, M., "Propeller Performance Data at Low Reynolds Numbers," AIAA Paper 2011-1255, 2011. doi:10.2514/6.2011-1255

[29] Gur, O., and Rosen, A., "Propeller Performance at Low Advance Ratio," *Journal of Aircraft*, Vol. 42, No. 2, 2005, pp. 435–441. doi:10.2514/1.6564

[30] Li, L., and Hu, H., "An Experimental Study of Dynamic Ice Accretion Process on Aero-Engine Spinners," AIAA Paper 2017-0551, 2017. doi:10.2514/6.2017-0551

[31] Liu, Y., and Hu, H., "An Experimental Investigation on the Unsteady Heat Transfer Process over an Ice Accreting Airfoil Surface," *International Journal of Heat and Mass Transfer*, Vol. 122, 2018, pp. 707–718. doi:10.1016/j.ijheatmasstransfer.2018.02.023

[32] Waldman, R. M., and Hu, H., "High-Speed Imaging to Quantify Transient Ice Accretion Process over an Airfoil," *Journal of Aircraft*,

Vol. 53, No. 2, 2016, pp. 369–377.
doi:10.2514/1.C033367

[33] Hansman, R. J., Yamaguchi, K., Berkowitz, B., and Potapczuk, M., "Modeling of Surface Roughness Effects on Glaze Ice Accretion," *Journal of Thermophysics and Heat Transfer*, Vol. 5, No. 1, 1991, pp. 54–60.
doi:10.2514/3.226

[34] Özgen, S., and Canıbek, M., "Ice Accretion Simulation on Multi-Element Airfoils Using Extended Messinger Model," *Heat and Mass Transfer*, Vol. 45, No. 3, 2009, pp. 305–322.
doi:10.1007/s00231-008-0430-4

[35] Anderson, D., "Acceptable Tolerances for Matching Icing Similarity Parameters in Scaling Applications," AIAA Paper 2001-0832, 2001.
doi:10.2514/6.2001-832

A. K. Gupta
Associate Editor